Contents lists available at ScienceDirect

Journal of Materiomics

journal homepage: www.journals.elsevier.com/journal-of-materiomics/

Extremely stable Li-metal battery enabled by piezoelectric polyacrylonitrile quasi-solid-state electrolytes

Hongzhi Peng [a], Zhong Xu [a], Yunjie Zhou [b], Junfeng Huang [a], Tao Yang [a], Jieling Zhang [a], Yong Ao [a], Yanting Xie [a], Hanyu He [a], Xiong Zhang [c], Weiqing Yang [a], Haitao Zhang [a, *]

[a] *Key Laboratory of Advanced Technologies of Materials, Ministry of Education, School of Materials Science and Engineering, Southwest Jiaotong University, Chengdu, 610031, China*
[b] *Chengdu Metro Operation No. 3 Company, Chengdu, 610031, China*
[c] *Institute of Electrical Engineering, Chinese Academy of Sciences, Beijing, 100190, China*

ARTICLE INFO

Article history:
Received 1 February 2023
Received in revised form
25 April 2023
Accepted 27 April 2023
Available online xxx

Keywords:
Polymer solid-state electrolytes
Polyacrylonitrile
Piezoelectric effect
Lithium metal battery
Long-term stability
Lithium dendrites

ABSTRACT

Polymer solid-state electrolytes (PSSEs) are promising for solving the safety problem of Lithium (Li) metal batteries (LMBs). However, PSSEs with low modulus in nature are prone to be penetrated by lithium dendrites, resulting in short circuit of LMBs. Here, we design and prepare piezoelectric $BaTiO_3$ doped polyacrylonitrile (PAN@BTO) quasi-solid-state electrolytes (PQSSEs) by electrostatic spinning method to suppress dendritic growth. The piezoelectric polymer electrolytes are squeezed by nucleation and growth processes of Li dendrites, which can generate a piezoelectric electric field to regulate the deposition of Li^+ ions and eliminate lithium bud. Consequently, piezoelectric PAN@BTO PQSSEs enables highly stable Li plating/stripping cycling for over 2 000 h at 0.15 mA/cm^2 at room temperature (RT, 25 °C). Also, $LiFePO_4$|PAN@BTO|Li full cells demonstrate excellent cycle performance (136.9 mA·h/g and 78% retention after 600 cycles at 0.5 C) at RT. Moreover, $LiFePO_4$|PAN@BTO|Li battery show extremely high safety and can still work normally under high-speed impact (2 Hz, ~30 kPa). We construct an *in-situ* cell monitoring system and disclose that the mechanism of suppressed lithium dendrite is originated from the generation of opposite piezoelectric potential and the feedback speed of intermittent piezoelectric potential signals is extremely fast.

1. Introduction

Lithium metal is considered as one of the most promising anode materials due to its high theoretical specific capacity (3860 mA·h/g) and the lowest electrochemical potential (−3.04 V *vs.* standard hydrogen electrode) [1–4]. However, Li metal anode for lithium-metal batteries (LMBs) still faces notable challenges in practical application. The main problem is huge volume expansion during repeated Li^+ ions plating and stripping cycles on Li anode which would induce uncontrolled dendrites growth [5–7]. Sharply Li dendrites growth lead an internal short circuit, flammability and even an explosive catastrophe in liquid Li-ion batteries (LIBs) [8–10]. Therefore, it is particularly important to obtain extremely stable LMBs with high-safety by preventing Li dendrite growth.

Artificial SEI film, modified composite separator and 3D frame work have been explored for suppressing dendrite growth in LIBs by protecting and stabilizing Li metal anode [11–13]. As an alternative, solid-state electrolytes (SSEs) can replace organic liquid electrolyte to solve the safety problem of flammable and explosive issues [14]. Polymer SSEs (PSSEs) exhibit superior flexibility compared with inorganic electrolytes and can accommodate to the volume expansion of Li metal anode. On the other hand, its relatively higher mechanical modulus compared to nonaqueous electrolytes facilitates to inhibit the growth of lithium dendrites. Therefore, PSSEs are considered to be potential candidates for practical application in LMBs. However, PSSEs inhibiting lithium dendrite growth by mechanical barrier do not meet the expectations of researchers. Li dendrites are prone to penetrate into soft PSSEs due to the lack of enough high modulus (~6 GPa), leading to battery failure [15]. For instance, elastic modulus of PEO-based electrolytes is approximately 2–3 orders of magnitude lower than that of metallic Li. Therefore, PEO@LiTFSI electrolyte is easily

---

* Corresponding author.
E-mail address: haitaozhang@swjtu.edu.cn (H. Zhang).
Peer review under responsibility of The Chinese Ceramic Society.

https://doi.org/10.1016/j.jmat.2023.04.011

Please cite this article as: H. Peng, Z. Xu, Y. Zhou *et al.*, Extremely stable Li-metal battery enabled by piezoelectric polyacrylonitrile quasi-solid-state electrolytes, Journal of Materiomics, https://doi.org/10.1016/j.jmat.2023.04.011

punctured by Li dendrites after 38 h of polarizing at a low current density of 0.05 mA/cm^2 [16]. Therefore, it is still urgent to find some alternative solutions to the problem of lithium dendrites in PSSEs.

The construction of polymer-based composite electrolytes is a common strategy to enhance its mechanical strength and ionic conductivity [17–20]. For instance, Huo *et al.* designed a sandwich-type PSSEs by integrating $Li_{6.4}La_3Zr_{1.4}Ta_{0.6}O_{12}$ into polymer, it enabled stable Li plating/stripping cycling for over 400 h at 0.2 mA/cm^2 [21]. Zhang *et al.* proposed a novel low-enthalpy and high-entropy PEO-based electrolyte by introducing perovskite quantum dots and largely breaking the polymer chain to realize highly cycled (>1 000 h at 0.3 mA/cm^2) LMBs [22]. In addition, crosslinked electrolytes, interface coating, single-ion solid polymer electrolytes *etc.* are also developed to inhibit the Li dendrite growth [23–25]. Recently, a novel method of using piezoelectric effect to inhibit the growth of lithium dendrites has been proposed. Guang *et al.* used piezoelectric polarized PVDF film as the diaphragm of liquid lithium metal battery, which effectively inhibited the growth of lithium dendrites [26]. However, the method of suppressing lithium dendrite by piezoelectric effect still faces some unresolved problems: (1) the research on piezoelectric effect regulating Li^+ ion deposition is mainly in liquid batteries while there is rarely report in solid-state batteries [27], such as how to regulate the lithium ion deposition; (2) the exact piezoelectric mechanism influence on the electrochemical performance of the battery needs to be further studied. Therefore, it is urgent to develop novel piezoelectric polymer electrolytes to regulate lithium-ion deposition and study the underlying mechanism.

Herein, we report piezoelectric PAN@BTO PQSSEs that can effectively inhibit the growth of lithium dendrites and achieve uniform platting and stripping of Li^+ ions. By controlling the direction of piezoelectric potential generation near the metal Li anode, the influence mechanism of the piezoelectric electric field on the electrochemical performance of the battery was studied. When a piezoelectric electrolyte creates a positive electric potential near the metal Li anode electrode, piezoelectric effect can effectively prevent Li^+ ions deposition to the dendrite tip and promote uniform lithium deposition. As a result, Li|PAN@BTO|Li batteries present stable plating/stripping behavior (> 2 000 h under 0.15 mA/cm^2). Quasi-solid-state $LiFePO_4$|PAN@BTO|Li achieves excellent rate performance and cycle stability (136.9 mA·h/g and 78 % retention after 600 cycles at 0.5 C).

2. Experimental

2.1. Chemicals and materials

Polyacrylonitrile powder (PAN, $M_w = 150\ 000$, Aladdin), $BaTiO_3$ (Aladdin, China), dimethylformamide (DMF, Sigma-Aldrich), and 1 mol/L lithium hexafluorophosphate ($LiPF_6$)/ethylene carbonate (EC): dimethylcarbonate (DMC) (Do Do Chem, China) were used directly after received.

2.2. Preparation of electrospun PAN@BTO membrane

The weight ration of 10% (in mass) BTO powders were dispersed in the DMF solution by ultrasound for 1 h. Then the PAN powders (17%, in mass) were added into the mixture with magnetic stirring at the temperature of 60 °C for 12 h to prepare a homogeneous electrospinning solution. The prepared spinning solution was poured into 10 mL plastic syringe with a needle that was connected to a positive charge for 13 kV. The distance between the tip of needle and the collection place was set to be 12 cm, and a constant flow rate of solution was 2 mL/h. The electrospun nanofibers were collected on aluminum foil. Then the electrospun PAN@BTO membrane was dried under vacuum at 60 °C for 12 h to remove the residual solvent.

2.3. Preparation of PAN and PAN@BTO composite electrolytes

The nanofiber membranes were processed to several small discs with a diameter of 22 mm by laser marking, and then transferred into an argon filled glove box (moisture level <0.000 1%, in volume). PAN and PAN@BTO membrane were immersed in a liquid electrolyte solution of 1 mol/L $LiPF_6$/EC: DMC for about 5 min. Then the nanofiber membranes filled with liquid electrolyte were placed in the glove box for 48 h to remove residual liquid electrolyte. PAN and PAN@BTO electrolytes had an average thickness of 151 μm.

2.4. Preparation processes of the PAN@BTO-S and PAN@BTO-P

Electrospinning can produce a fixed polarization direction for PAN@BTO electrolyte, and PAN@BTO electrolyte was collected on the tin foil. Therefore, we named the front surface of electrolyte is the "+" and the back surface (close to the tin foil) is the "-". During battery assembly, when the front surface ("+") of PAN@BTO electrolyte contacts Li anode, named PAN@BTO-S. On the contrary, when the close to the tin foil surface ("-") of PAN@BTO electrolyte contacts Li anode, named PAN@BTO-P.

2.5. Fabrication of sensor patches

In order to manufacture a sensor, the nanofiber membrane was electroplated by magnetron sputtering (TPR450, China) silver onto the front and back for 5 min on each side. The membrane with Li salts used thin stainless steel as electrodes on each side. Then the nanofiber membrane was sandwiched between two thin carbon tapes serving as top and bottom electrodes. The polyurethane (PU) film covered on the device to protect from any external mechanical damage.

2.6. Characterizations

The material morphology was characterized by field-emission scanning electron microscope (SEM, JFOF JSM-7800 F) and transmission electron microscope (TEM, JEM-2100 F). EDS mapping was checked with a JEM-2100 F. To acquire the crystallinity variation of the materials, X-ray diffraction (XRD) spectra were recorded on a power X-ray diffraction (PANalytical X'pert, Cu K_α, 0.154 056 nm). Fourier transform infrared (FT-IR) spectra were recorded with a Thermo Fisher company Nicolet iS10 infrared instrument, applying the reflection and transmission patterns. Electrical signals of membranes were obtained with a keithley-6514 system electrometer, and signal was collected and analyzed by a data acquisition card (Ni PCL-6221). XPS conducted on a Thermo Scientific™ K-Alpha^{TM+} spectrometer equipped with a monochromatic Al K_α X-ray source (1 486.6 eV) operating at 100 W.

2.7. Electrochemical measurements

The electrochemical properties of the samples were studied using CR2032-type coin cells. Linear sweep voltammetry (LSV) was conducted with the Li|PQSSEs|SS (SS: stainless steel) cell at a scan rate of 10 mV/s from 0 to 6 V (*vs.* Li^+/Li). The electrochemical impedance spectroscopy (EIS) of the symmetric SS|PQSSEs|SS cell and full cells were collected on an electrochemical workstation (CHI660E, Shanghai, China). The amplitude was 5 mV, the frequency ranged from 10^6 to 1 Hz, and the temperature was controlled using an environmental chamber (T-HWS-150H, Dongguan, China) between ambient temperature and 60 °C. Cyclic voltammetry (CV) was conducted with the Li|PQSSEs|LFP cell with different scanning rates in the voltage range of 2.5–4.2 V. Galvanostatic cycling of the Li|PQSSEs|Li symmetric cell was conducted at a current density of 0.15 mA/cm^2 (cycled at 25 °C). Both the charge and discharge times were 0.5 h. The rate capacity and cycling performance of the PSSEs were evaluated using LFP|PQSSEs|Li all-solid-state batteries through a computer-controlled battery tester system (Neware CT2100) at rate of 0.1 C, 0.2 C, 0.5 C, 1.0 C in the voltage range of 2.5–4.2 V.

2.8. *Preparation of in-situ cells*

The cell was sealed with Al-plastic film. For simultaneous monitoring, we designed four tabs for each cell and they can connect with the cathode and anode and hence connect electrochemical workstation and 6514 equipment for collecting data.

2.9. *Preparation of LiFePO$_4$ electrodes*

LiFePO$_4$ (LFP) electrodes were prepared by a typical procedure. Simply, dehydrated LFP, Super P, and polyvinylidene fluoride solution (4% (in mass) in N-methyl pyrrolidone) at a mass ratio of 85:10:5 was mixed with a moderate amount of N-methyl pyrrolidone under ball-mill stirring at 400 r/min for 4 h. The electrodes were made by doctor blading on aluminum foil. For drying electrodes, the electrodes were dried under vacuum for 12 h at 120 °C. After drying, the electrodes were punched into disks with a diameter of 6 mm prior to use.

3. Results and discussion

Fig. 1 shows the inhibited growth of lithium dendrites in piezoelectric PAN@BTO PQSSEs. During plating/stripping processes, dendrite nucleation occurs first at the lithium anode. Then, Li$^+$ ions accumulate and deposit at the nucleation site due to tip effect, which leads to the formation of lithium dendrites (the left panel of Fig. 1). Taking into piezoelectric effect into consideration, the stress originated from the process of dendrite growth would deform the polarized PAN@BTO PQSSEs, which generated instantaneous positive and negative charges on the surface of PQSSEs. In this regard, an internal electric filed was induced by heterocharges. The internal electric filed can effectively prevent Li$^+$ ions from further deposition to the dendrite tip, which is beneficial to the homogenization of the Li$^+$ ion transport flux (the middle panel of Fig. 1). Therefore, the dendrite growth in the vertical direction is effectively prevented and lithium dendrite is eliminated in the bud stage, so that dendrite-free Li-metal solid-state battery with excellent cycling stability would be anticipated (the right panel of Fig. 1).

Piezoelectric PAN@BTO films were prepare by electrospinning as shown in Fig. 2a. Due to strong electric field polarization and strong tensile effect, the dipoles in PAN@BTO films could be aligned internally. Through controlling electrospinning parameters like spinning time and spinning distance, the size and thickness of PAN@BTO films were adjusted efficiently. A typical PAN@BTO film with a large area of ~400 cm^2 was shown in Fig. 2b. Fig. 2c presents an optical image of PAN@BTO film bundles rolled around a cylindrical plastic with a diameter of 2.5 mm, indicating its highly flexible and foldable characteristics. This one-step, large-scale, and controllable spinning technology of preparing piezoelectric PAN@BTO film is expected to achieve commercial application.

The microstructures of piezoelectric PAN@BTO films were characterized by scanning electron microscopy (SEM) (Fig. 2d). The nanofibers in the PAN@BTO films were interwoven arbitrarily to form a three-dimensional network structure. Noted that there is no polymer beads or residual solvents, indicating spinning film possesses high-quality. Similar to pure PAN film (Fig. S1a), PAN@BTO show nearly equivalent size and morphology, demonstrating the addition of BTO do not damage the structure of PAN fiber itself. The signals of element N in PAN and Ti, Ba, and O in BTO are uniformly distributed (Fig. S1b), indicating that the BTO nanoparticles were uniformly dispersed in the composite film without obvious agglomeration. Through statistical analysis, the average fiber diameter of PAN@BTO film is 454 nm (Fig. 2e), which is slightly higher than that of pure PAN film with an average diameter of 449 nm (Fig. S1c). The uniformity of fiber diameter is also slightly decreased, which may be due to the slightly increased viscosity of spinning solution caused by the addition of BTO particles. The transmission electron microscopy (TEM) and SEM images of BTO particles show that the diameter of most nanoparticles is less than 500 nm (Fig. 2f and Fig. S1d) that are suitable to be embedded into the PAN fiber tube (Fig. 2g). From X-ray diffraction (XRD) characterization, PAN@BTO films exhibit five extra sharp diffraction peaks between 10° and 50° (Fig. 2h) that are matched well with pure BTO.

sample (Fig. S2). Particularly, two splitting peaks (002) and (200) are obviously found in near 45°; they belong to the characteristic peak of tetragonal phase BTO [28,29]. Due to high piezoelectric coefficient of tetragonal phase BTO and local stress enhancement of composite film by BTO particles, the synergistic piezoelectric effect of both BTO particles and PAN would enable

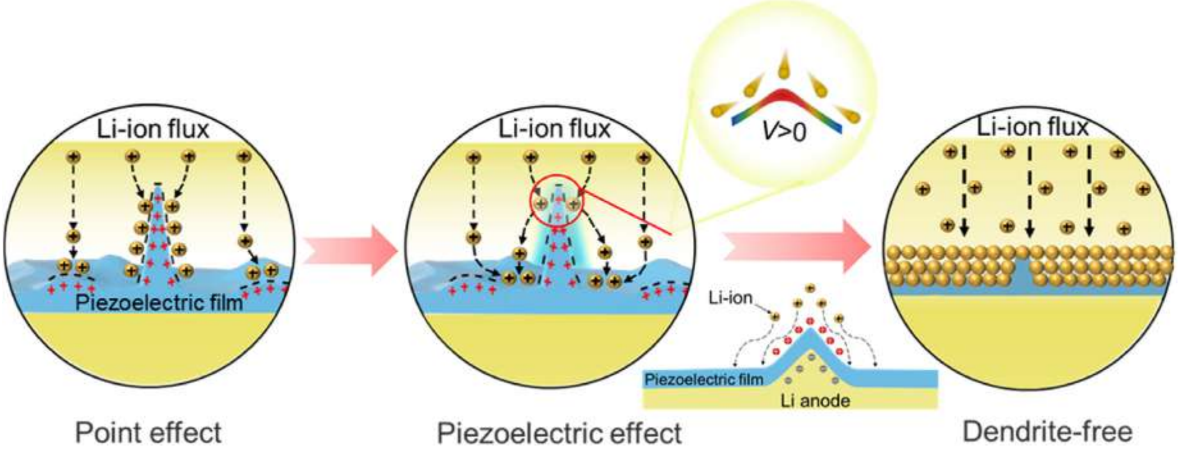

Fig. 1. Schematically illustrating piezoelectric effect in PAN@BTO electrolytes to realize homogenous Li deposition.

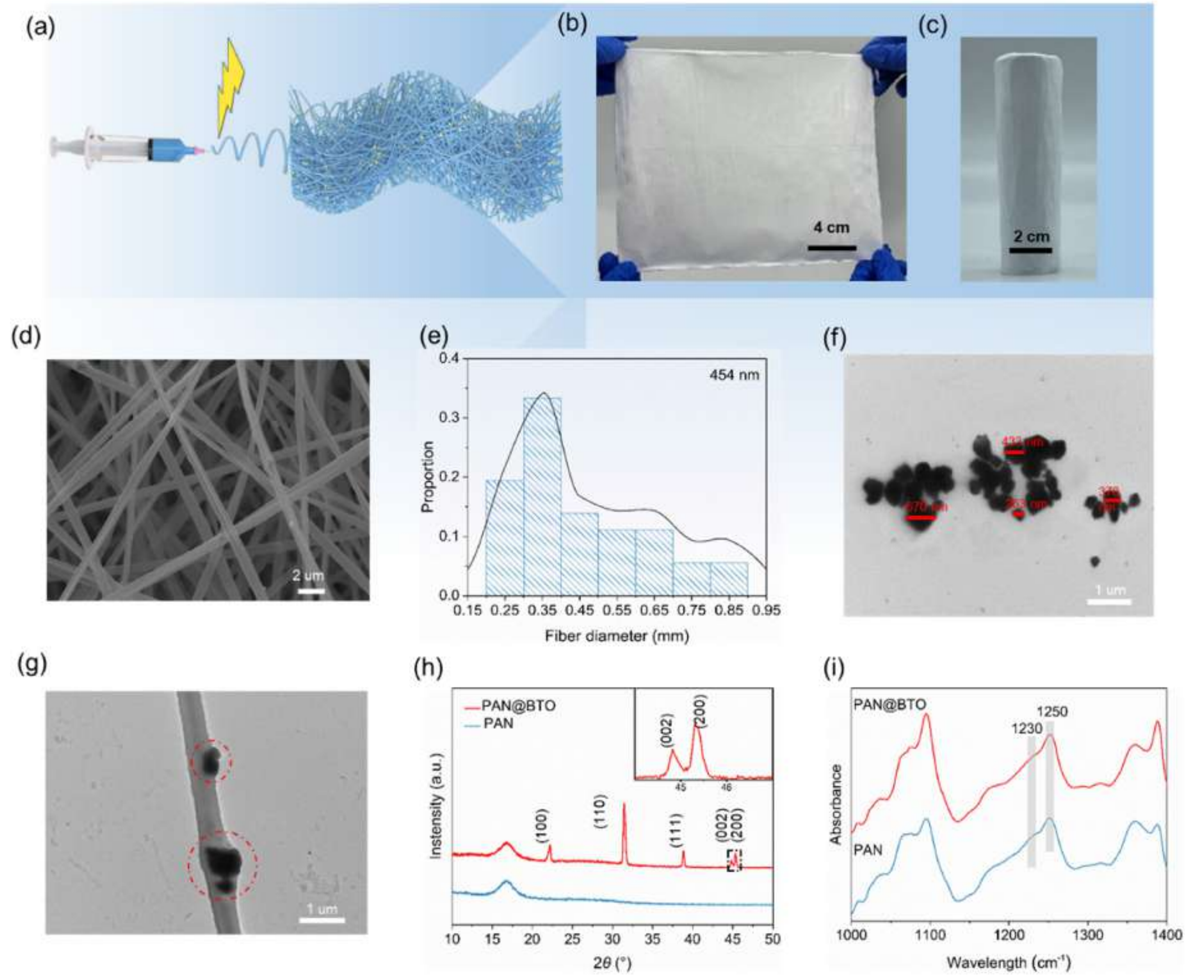

Fig. 2. Preparation and microstructures of PAN@BTO films. (a) Electrospinning method to produce PAN@BTO film. Optical image of PAN@BTO film (b) in planar, and (c) in foldable state. (d) SEM images of PAN@BTO film. (e) Diameter distribution histogram of PAN@BTO nanofibers. TEM images of (f) BTO nanoparticls and (g) PAN@BTO nanofibers. (h) XRD pattern. (i) FTIR spectra of the PAN@BTO film.

piezoelectric PAN@BTO film to have higher electrical output performance.

Fig. 2i shows the FTIR spectra of the PAN and PAN@BTO films. The vibration bands at 1 250 cm^{-1} and 1 230 cm^{-1} are corresponded to the zigzag conformation and 3_1-helical conformation, respectively. The presence of zigzag conformation indicates PAN large dipole moment that is good for piezoelectricity [30]. The content of the planar zigzag conformation can be estimate by Eq. 1

$$Q = S_{1230}/S_{1250} \tag{1}$$

where S_{1230} and S_{1250} are the peak area at 1 230 cm^{-1} and 1 250 cm^{-1}, respectively. PAN/BTO film has a Q of 0.77, which is lower than those of pure PAN film ($Q = 0.96$) (more detailed comparison can be found in Figs. S3a–b), indicating that the addition of BTO nanoparticles can promote the transformation of the 3_1-helical conformation to the zigzag conformation. In short, PAN@BTO film exhibited superior piezoelectric properties than pure PAN film.

To further study the piezoelectric performance of PAN and PAN@BTO film, the electrical voltage output of the nanofiber sensor with the PAN and PAN@BTO films was detected by a periodic impacting/releasing machine. In pressing mode, the cycle output voltage of pure PAN films is only increased from 0.28 V to 1.2 V as the pressure is changed from 1.23 to 11.24 N (Fig. 3a). What is worse, the voltage sensitivity decreases obviously when the force is greater than 8 N (Fig. S4a). In contrast, the PAN@BTO films show higher voltage output performance, especially at lower force. The cycle output voltage of PAN@BTO films reaches 0.8 V that is 3 times of pure PAN film under 1.22 N. When the force continues to increase to 11.06 N, the output voltage of PAN@BTO films exhibits a cycle voltage output of 1.6 V. Moreover, PAN@BTO films can maintain a high voltage sensitivity during the period of force from 1.22 to 11.08 N (Fig. S4b). All in all, the addition of BTO can effectively improve the piezoelectric properties of PAN, indicating that BTO particles contribute to the production of serrated conformation in PAN.

Meanwhile, the addition of BTO also improves the mechanical strength of PAN films (5.2 *vs.* 3.6 MPa, Fig. 3c). The increase of Young's modulus is probably due to the clustering effect of BTO and higher modulus can also enhance the piezoelectric output performance of PAN [31]. In order to verify whether the PAN@BTO electrolyte can maintain good piezoelectric output performance after immersion, we conducted the same test on the piezoelectric sensor made of dried PAN@BTO electrolyte. The nanofiber sensor showed the same typical voltage output, which could show a voltage output close to 1 V at 5 N (Fig. 3d). Furthermore, PAN@BTO membranes can exhibit long-term stability over 2 000 dynamic loading cycles (Fig. 3e), indicating that piezoelectric PAN@BTO electrolytes can be

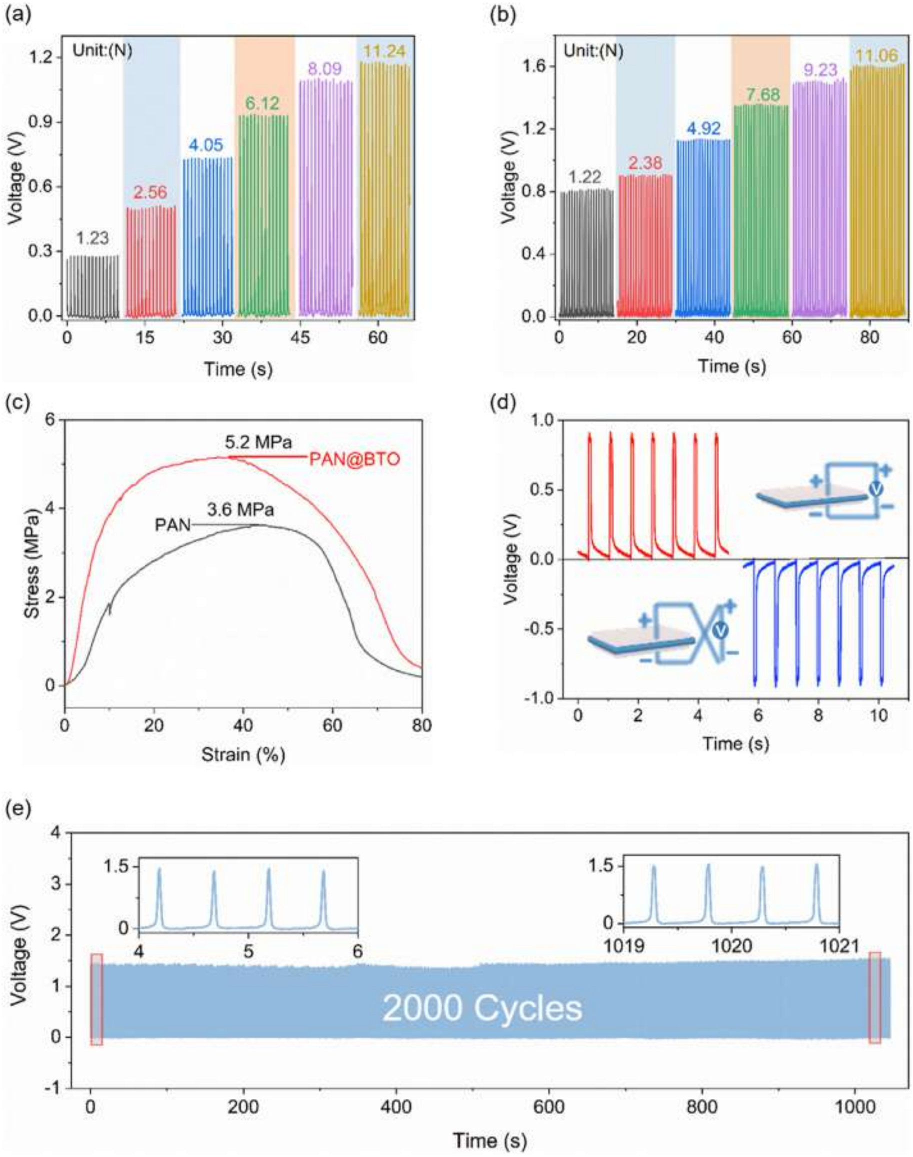

Fig. 3. Piezoelectric and mechanical properties of PAN@BTO films. Output voltage of (a) pure PAN and (b) PAN@BTO films under different forces. (c) Representative stress-strain curves of PAN and PAN@BTO films. (d) The measured voltage signals from the forward and reverse connections of PAN@BTO electrolytes. (e) PAN@BTO films exhibited long-term stability under continuous force load.

used stably in LMBs.

Various electrochemical measurements were tested to evaluate the feasibility of PAN@BTO PQSSEs used in LMBs. Ionic conductivity, a crucial parameter in PQSSEs, was first determined. PAN@BTO electrolyte exhibit higher ionic conductivity at the temperature ranging from 25 to 60 °C. As shown in Fig. 4a, the ionic conductivity of PAN@BTO electrolyte (~1.8×10^{-4} S/cm) was nearly two orders of magnitude higher than that of pure PAN electrolyte (~2×10^{-6} S/cm) at 25 °C (ionic conductivity at different temperatures in Table S1). The increased ionic conductivity is contributed to faster Li^+ ions transport by the reduction of polymer crystal area (X_c% from 75.3% decrease to 61.5%, more details was shown in Fig. S5). The reasons of decreased crystallinity are as follows: (1) the H atom of hydroxyl group on the surface of BTO nanoparticles form a strong hydrogen bond with the N atom in PAN during the spinning process [32]; (2) The presence of BTO nanoparticles can restrict the movement of the polymer chains. Although the ionic conductivity is significantly improved, the electrochemical window is almost similar. The electrochemical window of the electrolyte membranes was studied by liner sweep voltammogram (LSV) method. During the voltage range of 2.0–5.2 V, PAN@BTO and pure PAN exhibit electrochemical stable window of 4.7 and 4.8 V, respectively, at a scan rate of 1 mV/s (Fig. 4b). The slight decrease in electrochemical stable window after introducing BTO could be attributed to the extra ceramic/polymer interface that would bring in additional interfacial issue. Meanwhile, the lithium-ion migration number of PAN@BTO electrolyte was calculated by EIS and dc polarization at ambient temperature. In Fig. S6, the PAN@BTO electrolyte exhibits potent ability of lithium ion migration, whose calculated number is 0.54. Desirable transference number can improve the homogeneous Li^+ deposition [33,34].

The piezoelectric PQSSEs deformation through nucleation of dendrite protrusion to generate positive electric potential, so as to offset the overpotential caused by tip effect and prevent deposition of Li^+ ions to the tip. Theoretically, the direction of the electric filed generated by the polarized PQSSEs will play a decisive role in the

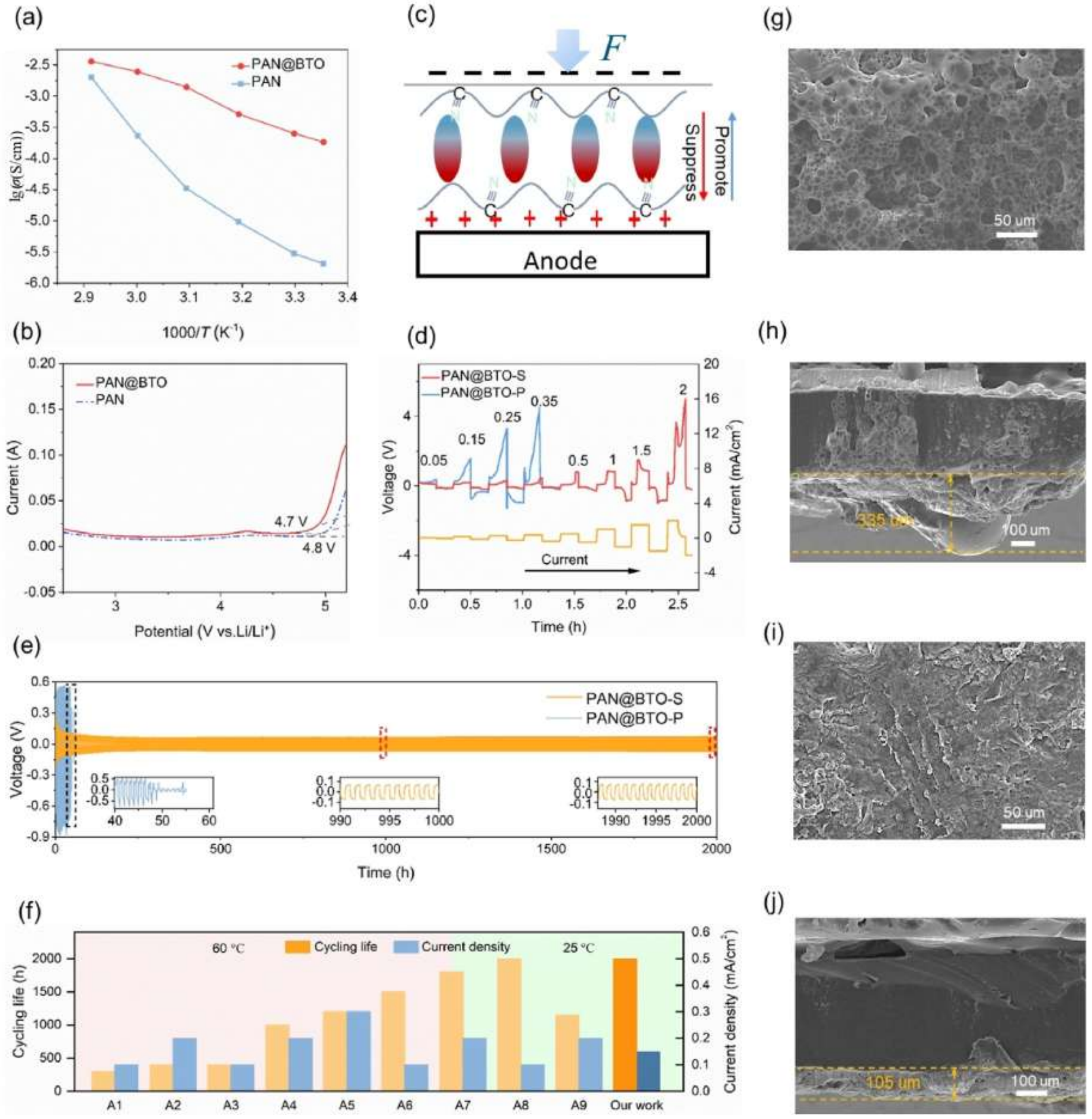

Fig. 4. Electrochemical properties of piezoelectric polymer PQSSEs and their-based Li| | Li symmetric batteries. (a) Temperature-dependence ionic conductivity of PAN and PAN@BTO PQSSEs. (b) LSV of PAN and PAN@BTO PQSSEs. (c) The direction of the polarized electrolyte influences the direction of piezoelectric potential on the growth of lithium dendrites. (d) The voltage profiles of the two Li || Li symmetric batteries with increased current density. (e) Cycling stability of Li|PAN@BTO-S|Li and Li|PAN@BTO-P|Li batteries at a current density of 0.15 mA/cm^2 at 25 °C. (f) Cycling life and corresponding current density of different PQSSEs. Top-view and cross-sectional SEM images of Li anode after cycling with (g and h) PAN@BTO-P and (i and j) PAN@BTO-S PQSSEs.

growth of lithium dendrites. When the piezoelectric PQSSEs generate positive charge near the anode, it had the ability to suppress the growth of lithium dendrites, named PAN@BTO-S. Conversely, it is responsible to accelerate the growth of lithium dendrites when piezoelectric PQSSEs generate negative charge near the anode, named PAN@BTO-P. Hence, we changed the direction of the polarized electrolyte placement to achieve the purpose of controlling the electric potential output direction (more preparation processes in Fig. S7), focusing on the influence of the piezoelectric potential direction on the growth of lithium dendrites.

Fig. 4d shows the voltage profiles of the two lithium symmetric cells with the increased current. Initially, Li|PAN@BTO-P|Li cell showed a higher polarization voltage at a current density of 0.05 mA/cm^2. Furthermore, Li|PAN@BTO-P|Li cell.

exhibited a serious abnormal overpotential conversion when the current density gradually increased to 0.15 mA/cm^2, which would lead to battery failure. On the contrary, Li|PAN@BTO-S|Li cell still showed a small voltage polarization and stable voltage range even when the current density was largely increased to 0.35 mA/cm^2. Ultimately, Li|PAN@BTO-S|Li battery failed as the current density increased to a very high current density of 2 mA/cm^2. A similar phenomenon was found on Li|PAN|Li symmetric cell, where Li|PAN-S|Li cell exhibited much lower polarization voltage at the same current density (Fig. S8 and Figs. S9a–b). In addition, Li|PAN@BTO-S|Li cell presents an excellent stability over 2 000 h while Li|PAN@BTO-P|Li can cycle only for 50 h at a current density of 0.15 mA/cm^2 (Fig. 4e), meaning that the battery has a fast short-circuit behavior. Similarly, Li|PAN-S|Li battery can stably cycle for more than 500 h, while the lifetime of Li|PAN-P|Li battery is only 50 h (Fig. S10). The plating/stripping performance of these assembled Li|PAN@BTO-S|Li cell were found to be better than those of polymer-based PSSEs recently reported (Fig. 4f) [35–44].

We also used XPS to discuss the interface compatibility between PQSSEs with Li anode. After cycling 1 000 h of Li|PAN@BTO-S|Li cell, LiN_3, Li_2O, LiF and $Li_xPO_yF_z$ were found at Li|PAN@BTO-S|Li cell interface (Fig. S11). The N 1*s* peak at 403.7 eV and O 1s peak at 530.7 eV corresponded to LiN_3 and Li_2O (Figs. S11a–b). The SEI mainly consists of inorganic LiN_3 and Li_2O which can form a strong compact and highly conductive passivation layer on the Li anode, thereby avoiding dendrite formation [45,46]. The O 1*s* peak (Fig. S11b) at 533.1 eV and F 1*s* peak (Fig. S11c) at 686.6 eV corresponded to $Li_xPO_yF_z$. As is known, LiF can help suppress the pentration of Li dendrites in to PQSSE. $Li_xPO_yF_z$ is as well-known electrolyte additive that has improved the cycling stabilities of lithium batteries [47,48]. Therefore, together with LiN_3, Li_2O, LiF and $Li_xPO_yF_z$ help in stabling the electrolyte/Li interface. Besides, other components at the interface included: C–O (C 1*s* peak at 285.2 eV) (Fig. S11d), C≡N, C≡N–Li^+ and NO_3^{-1} (N 1*s* peak at 399.7 eV, 402.1 eV and 407.2 eV respectively), C=O (C 1*s* peak at 289.7 eV, O 1s peak at 531.3 eV) [49]. C–O and C=O species are formed during cycling, indicating that some residual solvent decomposed. Therefore, piezoelectric effect plays a decisive role in stabilizing the interface between the PQSSEs and Li anode and hence suppressing the growth of lithium dendrites.

The morphologies of the lithium metal surface after cycling were confirmed by SEM characterization. After Li|PAN@BTO-P|Li battery is short circuited, the removed lithium anode has a rough surface containing mossy-like dendrite and prominent spherical dendrites with the maximum thickness of 335 μm (Fig. 4g-h). However, the lithium anode of Li|PAN@BTO-S|Li battery has a free-dendrite morphology, and the dense thickness of lithium anode surface is only 105 μm after 1 000 h (Fig. 4i-j). These results unambiguously indicate that when the piezoelectric electrolyte generates a positive piezoelectric potential at the dendrite nucleation site, it can greatly inhibit the growth of lithium dendrites, otherwise it will accelerate the growth and penetration of dendrites, leading to battery short circuit.

The LFP|PAN@BTO|Li batteries, where LFP is $LiFePO_4$, were assembled to investigate the electrochemical properties. LFP|PAN@BTO-S|Li battery showed flat voltage plateaus with unnoticeable polarization upon increasing current rates (Fig. 5a). In contrast, LFP|PAN@BTO-P|Li battery showed apparent voltage polarization and specific capacity degradation (Fig. 5b). LFP|PAN@BTO-S|Li battery delivered a specific capacity of 151 mA·h/g in the first cycle at 0.1C (Fig. 5c). At higher current densities of 0.2 and 0.5 C, the battery maintained specific capacity of 141.5 and 136.9 mA·h/g, respectively. Besides, the capacity of the battery could recover to the similar level of 0.1 C after high-rate cycling. In contrast, the first cycle specific capacity of LFP|PAN@BTO-P|Li at 0.1C was only 133.6 mA·h/g; and with the increase of current density, its capacity is always lower than that of LFP|PAN@BTO-S|Li battery. The low specific capacity could be attributed that the negative piezoelectric potential around the anode aggravated the nonuniformity of the SEI layer, leading to SEI rupture and uneven Li^+ ions deposition at the beginning of the battery cycle. LFP|PAN@BTO-S|Li batteries with positive piezoelectric effect maintain 88.2% capacity retention at 0.5C and 300 cycles (Fig. 5d), indicating good interface stability and compatibility. However, the capacity of LFP|PAN@BTO-P|Li battery with negative piezoelectric effect fluctuated sharply in the first 100 cycles. Subsequently, we shelved the LFP|PAN@BTO-S|Li battery for a month after 300 cycles. When we tested it again, LFP|PAN@BTO-S|Li battery still had an initial capacity of 98.4 mA·h/g at 0.5C. After 50 cycles, the battery capacity restored to 120.7 mA·h/g, which had an equal capacity to the battery (122.5 mA·h/g) before shelving. Finally, LFP|PAN@BTO-S|Li battery maintain 78% capacity retention (106.7 mA·h/g) at 0.5C after 600 cycles. The cycling performance of LFP|PAN@BTO-S|Li cell was found to be better than those of polymer-based PSSEs recently reported (Table S2)

In order to prove the safety performance of the LFP|PAN@BTO-S|Li battery, we applied a pressure with a frequency of 2 Hz and ~30 kPa to hit the cell continuously for 1 h (Fig. 5e). The recorded variation of battery voltage was shown in Fig. 5f. During charging process, the battery voltage suddenly changed at the moment as the initial force was applied, then the voltage of the lithium metal solid state battery returned to stability in the subsequent charging process. Although the battery voltage fluctuates increased strongly during the last impact, the whole charging process can still be completed. In the discharge process, under the external impact, the battery voltage had always tended to be stable finally. Impressively, it can deliver a specific capacity of.

126.9 mA·h/g at 0.5C, and the subsequent charging/discharging curves remain normal (Fig. S12). However, after the impact, the voltage of ordinary commercial liquid batteries fluctuated violently during the charging process, and soon reached the upper set limit of 4.2 V (Fig. 5g), which eventually led to battery failure. This result proves that the LFP|PAN@BTO-S|Li battery has high safety and can still work normally under high-speed impact. Therefore, as the piezoelectric PAN@BTO-S PQSSEs generate positive charge near the anode, it could enable Li metal battery extreme stability as summarized in Fig. 5h.

To disclose the work mechanism of piezoelectric effect on suppressing the lithium dendrites, we further prepared in-situ cells to simultaneously monitor the piezoelectricity and electrochemical performance. Fig. 6a schematically illustrates the structure of in-situ monitoring system. The different charge/discharge behavior of LFP|PAN@BTO-S|Li and LFP|PAN@BTO-P|Li cells was further analyzed by cyclic voltammetry (CV, Fig. 6b-c). The same anodic peak voltages (3.65 V) corresponding to $LiFePO_4 \leftrightharpoons Li_{1-x}FePO_4 + xLi^+ + xe^{-1}$ in CV curves are observed in two cells. Noted that a shoulder CV peak appears in LFP|PAN@BTO-P|Li cell, indicating the negative piezoelectric potential field would generate a hindrance of preventing the Li^+ ions deintercalation from $LiFePO_4$ electrode. This phenomenon is interesting while abnormal. It may lead to the formation of cathode electrolyte interphase and deteriorate the stability of LFP|PAN@BTO-P|Li cell. However, the exact mechanism for this abnormal behavior needs further investigation. In addition, the anodic and cathodic peaks of LFP|PAN@BTO-S|Li cell show a high symmetric overlap, indicating its excellent reversibility [50]. However, the anodic peaks area are far below cathodic peaks of LFP|PAN@BTO-P|Li cell, suggesting that the presence of an uneven solid-state interface induce hard for Li^+ ions to plat/strip [51].

Moreover, the electrochemical workstation was used to apply a constant current of 0.1 mA/cm^2 to the *in-situ* battery, so that Li^+ ions were continuously deposited in Li metal anode. LFP|PAN@BTO-P|Li voltage profile of the battery is recorded through 6514 equipment. In the process of Li^+ ions deposition, the nucleation and formation of lithium buds at the Li anode led to the deformation of the piezoelectric electrolyte and produced an instantaneous potential, which was successfully recorded by 6514 as shown in Fig. 6d. The generation of periodically piezoelectric signals imply that in the process of dendrite suppression, the dendrite growth is immediately suppressed after the potential generation. Moreover, the feedback speed is extremely fast, so regular intermittent piezoelectric potential signals can be displayed.

EIS plots of LFP|PAN@BTO|Li battery were tested to further study the interface between PAN@BTO electrolyte and electrode during cycling. The initial impedances of LFP|PAN@BTO-S|Li and LFP|PAN@BTO-P|Li batteries after assembly had little difference,

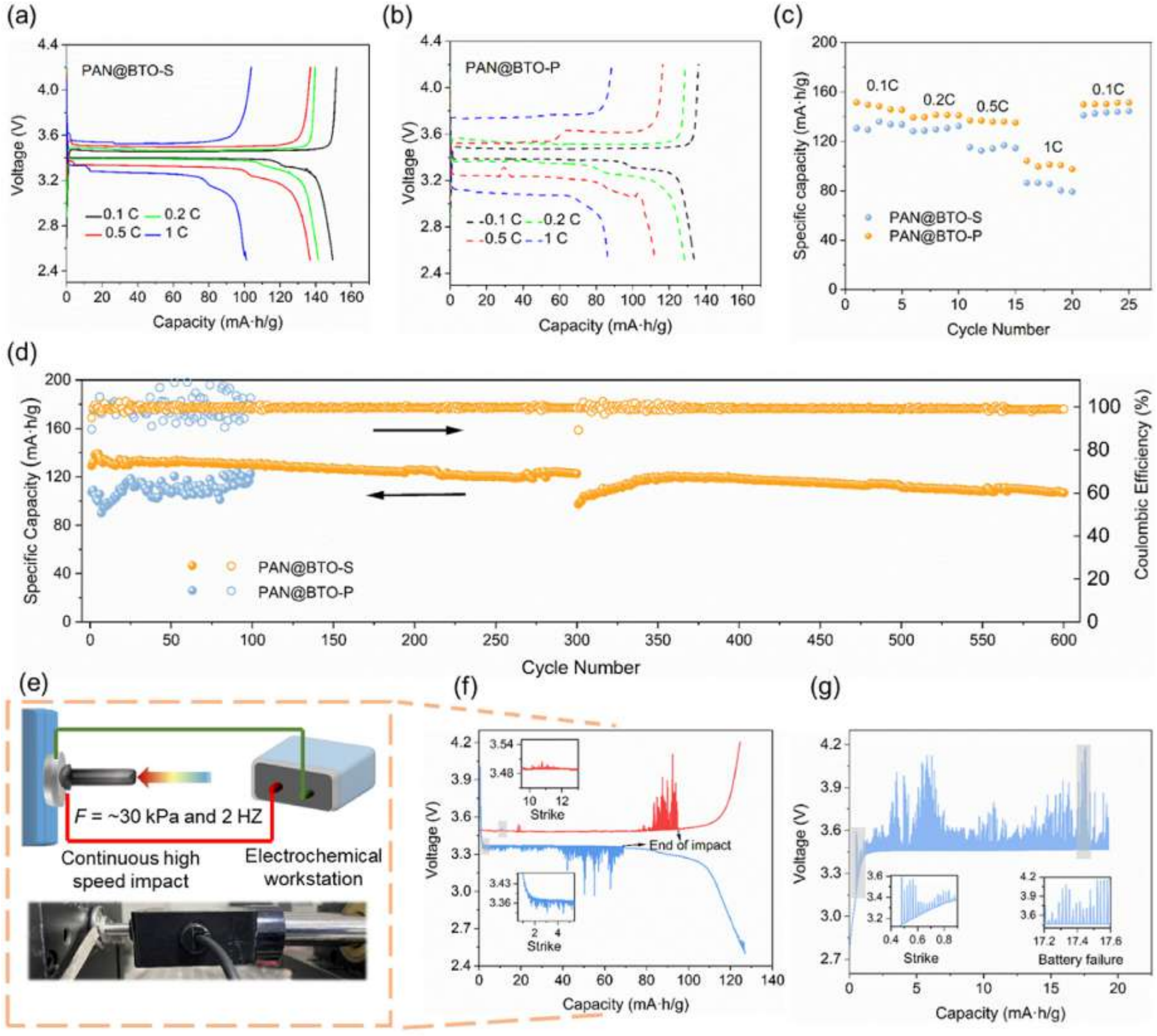

(h)

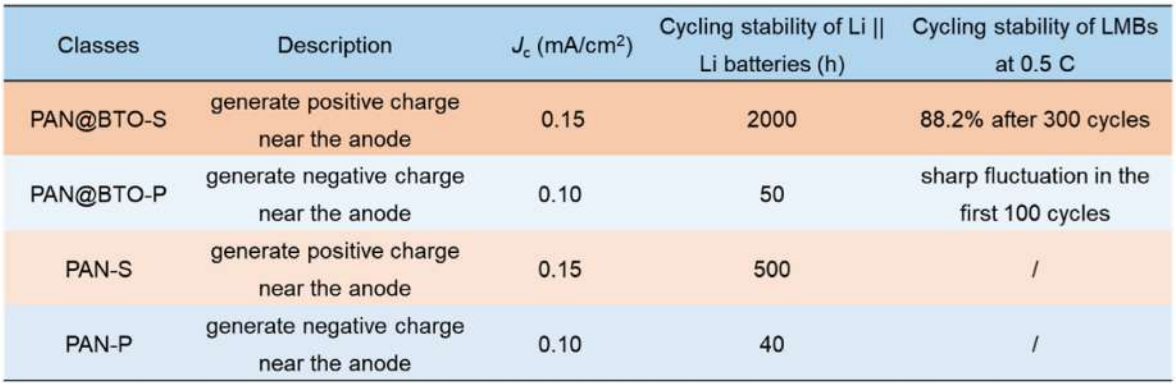

Classes	Description	J_c (mA/cm^2)	Cycling stability of Li || Li batteries (h)	Cycling stability of LMBs at 0.5 C
PAN@BTO-S	generate positive charge near the anode	0.15	2000	88.2% after 300 cycles
PAN@BTO-P	generate negative charge near the anode	0.10	50	sharp fluctuation in the first 100 cycles
PAN-S	generate positive charge near the anode	0.15	500	/
PAN-P	generate negative charge near the anode	0.10	40	/

Fig. 5. Electrochemical and mechanochemical properties of LFP|PAN@BTO|Li batteries. Charge/discharge profiles of (a) LFP|PAN@BTO-S|Li and (b) LFP|PAN@BTO-P|Li cells at current rates from 0.1C to 1 C (1 C = 170 mA·h/g. (c) Rate-capability of cells at various current rates. (d) Long-term cycling stability of the LFP|PAN@BTO-S|Li cell with a potential of 2.5–4.2 V at 0.5C and the corresponding Coulombic efficiency. (e) The voltage profiles of (f) LFP|PAN@BTO-S|Li and (g) Commercial liquid battery hit by a continuously external force with a frequency of 2 Hz and ~30 kPa for 1 h. (h) The summary of different typed piezoelectric PQSSEs constructed LMBs and their electrochemical properties.

which were 980 Ω and 1 050 Ω respectively (Fig. 6e). After the first cycle, the interface resistance of battery assembled with sandwiched LFP|PAN@BTO-S|Li rapidly decreased to 180 Ω, while that of LFP|PAN@BTO-P|Li battery only decreased to 680 Ω (Fig. 6f). Formation of SEI was conducive to increase the interface compatibility after the first cycle of the battery [52]. Meanwhile, LFP|PAN@BTO-S|Li battery helps to form a more compact SEI layer that greatly reduces the charge transfer resistance (R_{CT}). With the increase of cycles, the interface impedance of LFP|PAN@BTO|Li battery further decreased as shown in Fig. 6g-h. After 100 cycles, the R_{CT} of LFP|

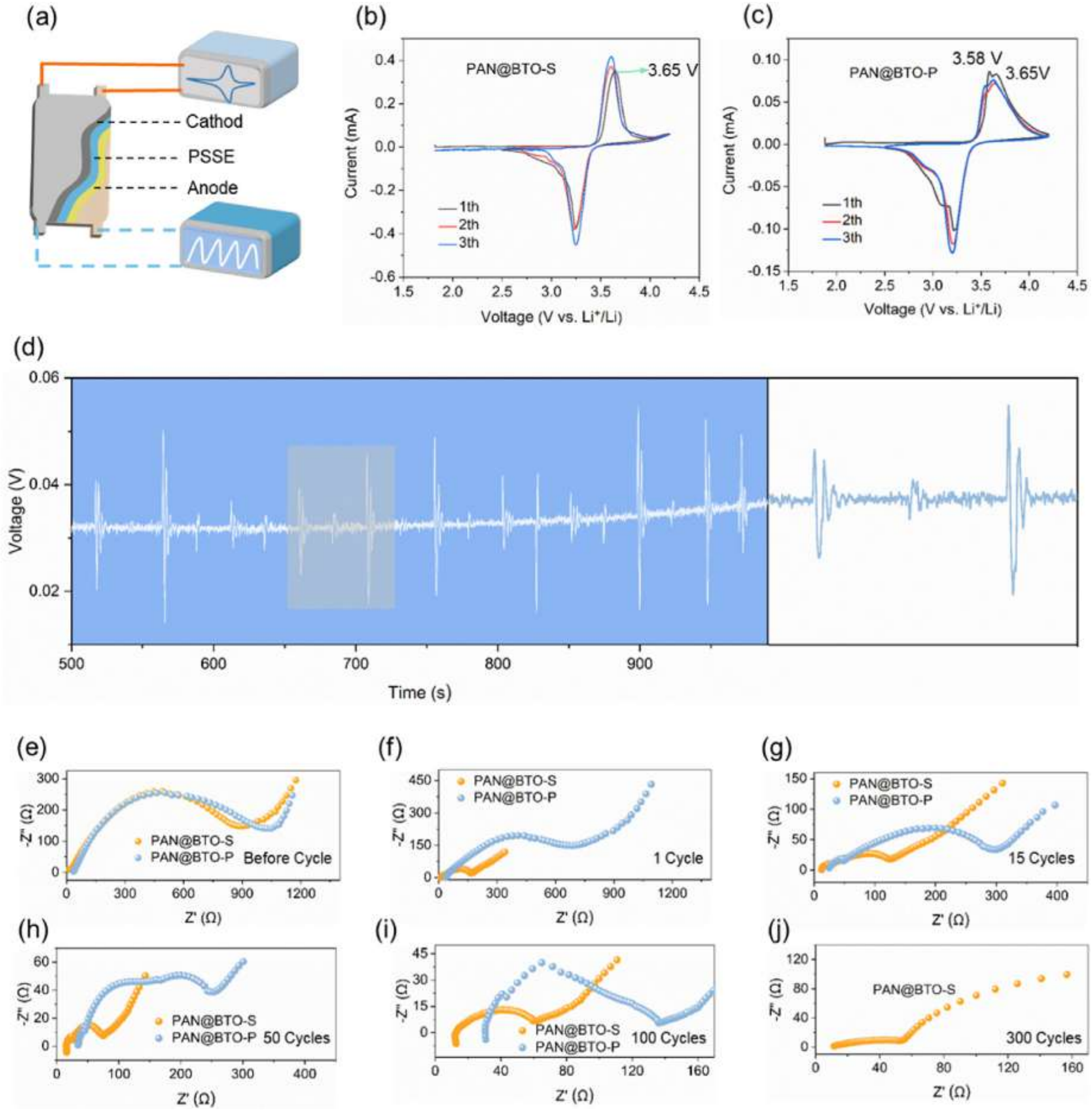

Fig. 6. Mechanism of piezoelectric effect stabilizes LMBs. (a) Designed in-situ system to monitor piezoelectricity and electrochemical properties simultaneously. CV curves of (b) LFP|PAN@BTO-S|Li and (c) LFP|PAN@BTO-P|Li batteries at a scanning rate of 0.1 mV/s. (d) Voltage profile of the *in-situ* cell. (e–j) EIS plots of LFP|PAN@BTO-S|Li and LFP|PAN@BTO-P|Li batteries during cycling.

PAN@BTO-S|Li and LFP|PAN@BTO-P|Li batteries decreased to 61 Ω and 116 Ω (Fig. 6i), respectively. After 300 cycles, LFP|PAN@BTO-S|Li battery only delivers a rather low R_{CT} of 52 Ω (Fig. 6j). These results further confirm that LFP|PAN@BTO-S|Li battery possesses good interfacial stability and superior compatibility against electrodes, which ascribed to the positive potential generated by piezoelectric effect is conducive to the formation of compact SEI layer and prevents the growth of lithium dendrites.

4. Conclusion

In conclusion, we designed piezoelectric PAN@BTO PQSSEs for suppressing lithium dendrite growth and stabilize lithium metal surface to build extremely stable lithium metal battery. This piezoelectric effect could enhance uniform deposition of Li^+ ions in Li metal anode and eliminate Li bud. Therefore, the outstanding electrochemical performance of all-solid-state LMBs were achieved. Li|PAN@BTO-S|Li symmetric battery exhibited outstanding electrochemical stability (>2 000 h under 0.15 mA/cm^2) and $LiFePO_4$|PAN@BTO-S|Li full cell achieves a specific capacity of 136.9 mA h/g at 0.5 C with high-capacity retention of 78% after 600 cycles. Moreover, the mechanism of piezoelectric electric field direction on suppressing dendrites growth is further disclosed. Piezoelectric PQSSEs generate positive charge near the anode, it can effectively suppress dendrites growth. Particular, the reason of enable Li metal battery extremely stable was comprehensively proved to be originated from piezoelectric effect of PQSSEs. This work provides a promising strategy to design piezoelectric polymer electrolyte for developing long-stable and high-safety lithium metal batteries.

Author contributions

Hongzhi Peng: Conceptualization, Methodology, Investigation, Writing-Review and Editing. Haitao Zhang: Supervision, Conceptualization, Methodology, Writing-Review and Editing, Funding Acquisition. Zhong Xu: Formal Analysis, Validation, Investigation. Yunjie Zhou: Investigation, Resources. Junfeng Hung: Investigation, Resources. Tao Yang: Methodology, Formal Analysis. Jieling Zhang: Investigation, Formal Analysis. Yong Ao: Methodology, Formal Analysis. Yanting Xie: Resources, Methodology. Hanyu He: Methodology, Validation. Xiong Zhang: Resources. Weiqing Yang: Funding Acquisition.

Declaration of competing interest

The authors declare that they have no known competing financial interests or personal relationships that could have appeared to influence the work reported in this paper.

Acknowledgements

This work is supported by the National Natural Science Foundation of China (Nos. 51977185, 51972277), and Natural Science Foundation of Sichuan Province (No. 2023NSFSC0441). The authors gratefully acknowledge the Analytical and Testing Center of Southwest Jiaotong University and Ceshigo (www.ceshigo.com) for providing the testing service.

Appendix A. Supplementary data

Supplementary data to this article can be found online at https://doi.org/10.1016/j.jmat.2023.04.011.

References

[1] Lee MJ, Han J, Lee K, Lee YJ, Kim BG, Jung KN, et al. Elastomeric electrolytes for high-energy solid-state lithium batteries. Nature 2022;601:217–22.

[2] Jin S, Sun Z, Guo Y, Qi Z, Guo C, Kong X, et al. High areal capacity and lithium utilization in anodes made of covalently connected graphite microtubes. Adv Mater 2017;29:1700783.

[3] Lin D, Liu Y, Cui Y. Reviving the lithium metal anode for high-energy batteries. Nat Nanotechnol 2017;12:194–206.

[4] Yan J, Yu J, Ding B. Mixed ionic and electronic conductor for Li-metal anode protection. Adv Mater 2018;30:1705105.

[5] Hou C, Han J, Liu P, Yang C, Huang G, Fujita T, et al. Operando observations of SEI film evolution by mass-sensitive scanning transmission electron microscopy. Adv Energy Mater 2019;9:1902675.

[6] Shi P, Fu ZH, Zhou MY, Chen X, Yao N, Hou LP, et al. Inhibiting intercrystalline reactions of anode with electrolytes for long-cycling lithium batteries. Sci Adv 2022;8. https://doi.org/10.1126/sciadv.abq3445.

[7] Liu Y, Lin D, Yuen PY, Liu K, Xie J, Dauskardt RH, et al. An artificial solid electrolyte interphase with high Li-ion conductivity, mechanical strength, and flexibility for stable lithium metal anodes. Adv Mater 2017;29:1605531.

[8] Yan K, Lee HW, Gao T, Zheng G, Yao H, Wang H, et al. Ultrathin two-dimensional atomic crystals as stable interfacial layer for improvement of lithium metal anode. Nano Lett 2014;14:6016–22.

[9] Zheng G, Lee SW, Liang Z, Lee HW, Yan K, Yao H, et al. Interconnected hollow carbon nanospheres for stable lithium metal anodes. Nat Nanotechnol 2014;9:618–23.

[10] Li W, Yao H, Yan K, Zheng G, Liang Z, Chiang YM, et al. The synergetic effect of lithium polysulfide and lithium nitrate to prevent lithium dendrite growth. Nat Commun 2015;6:1–8.

[11] Li S, Huang Y, Ren W, Luo C, Zhao L, Liu J, et al. An optimized 3D polymer alloy interface for durability and safety for Li metal batteries. Chem Eng J 2021;420:130002.

[12] Li S, Huang Y, Ren W, Li X, Wang M, Cao H. Stabilize lithium metal anode through in-situ forming a multi-component composite protective layer. Chem Eng J 2021;422:129911.

[13] Li S, Huang Y, Luo C, Ren W, Yang J, Li X, et al. Stabilize lithium metal anode through constructing a lithiophilic viscoelastic interface based on hydroxypropyl methyl cellulose. Chem Eng J 2020;399:125687.

[14] Lee N, Oh J, Choi JW. Anode-less all-solid-state batteries: recent advances and future outlook. Materials Futures 2023. https://doi.org/10.1088/2752-5724/acb3e8.

[15] Qi L, Wu Z, Zhao B, Liu B, Wang W, Pei H, et al. Advances in artificial layers for stable lithium metal anodes. Chem Eur J 2020;26:4193–203.

[16] Brissot C, Rosso M, Chazalviel JN, Lascaud S. Dendritic growth mechanisms in lithium/polymer cells. J Power Sources 1999;81:925–9.

[17] Shen Y, Zhang Y, Han S, Wang J, Peng Z, Chen L, et al. Unlocking the energy capabilities of lithium metal electrode with solid-state electrolytes. Joule 2018;2:1674–89.

[18] Armand M, Tarascon JM. Building better batteries. Nature 2008;451:652–7.

[19] Xu Z, Zhang H, Yang T, Chu X, Xie Y, Wang Q, et al. Physicochemically dendrite-suppressed three-dimensional fluoridation solid-state electrolyte for high-rate lithium metal battery. Cell Reports Physical Science 2021;2:100644.

[20] Tarascon JM, Armand M. Issues and challenges facing rechargeable lithium batteries. Nature 2001;414:359–67.

[21] Huo H, Chen Y, Luo J, Yang X, Guo X, Sun X. Rational design of hierarchical "ceramic-in-polymer" and "polymer-in-ceramic" electrolytes for dendrite-free solid-state batteries. Adv Energy Mater 2019;9:1804004.

[22] Zhang H, Wang Y, Huang J, Li W, Zeng X, Jia A, et al. Low-enthalpy and high-entropy polymer electrolytes for Li-metal battery. Eenergy Environ. Mater. 2023. https://doi.org/10.1002/eem2.12514.

[23] Liu Y, Xu B, Zhang W, Li L, Lin Y, Nan C. Composition modulation and structure design of inorganic-in-polymer composite solid electrolytes for advanced lithium batteries. Small 2020;16:1902813.

[24] Fan Z, Ding B, Zhang T, Lin Q, Malgras V, Wang J, et al. Solid/solid interfacial architecturing of solid polymer electrolyte–based all-solid-state lithium–sulfur batteries by atomic layer deposition. Small 2019;15:1903952.

[25] Cao C, Li Y, Chen S, Peng C, Li Z, Tang L, et al. Electrolyte-solvent-modified alternating copolymer as a single-ion solid polymer electrolyte for high-performance lithium metal batteries. ACS Appl Mater Interfaces 2019;11:35683–92.

[26] Liu G, Wang D, Zhang J, Kim A, Lu W. Preventing dendrite growth by a soft piezoelectric material. ACS Mater. Lett. 2019;1:498–505.

[27] Kang J, Yan Z, Gao L, Zhang Y, Liu W, Yang Q, et al. Improved ionic conductivity and enhancedinterfacial stability of solid polymer electrolytes with porous ferroelectric ceramic nanofibers. Energy Storage Mater 2022;53:192–203.

[28] Zhu P, Chen Y, Shi J. Piezocatalytic tumor therapy by ultrasound-triggered and $BaTiO_3$-mediated piezoelectricity. Adv Mater 2020;32:2001976.

[29] Alluri NR, Chandrasekhar A, Vivekananthan V, Purusothaman Y, Selvarajan S, Jeong JH, et al. Scavenging biomechanical energy using high-performance, flexible $BaTiO_3$ nanocube/PDMS composite films. ACS Sustainable Chem Eng 2017;5:4730–8.

[30] Hobson RJ, Windle AH. Crystalline structure of atactic polyacrylonitrile. Macromolecules 1993;26:6903–7.

[31] Kim HS, Lee DW, Kim DH, Kong DS, Choi J, Lee M, et al. Dominant role of Young's modulus for electric power generation in PVDF–$BaTiO_3$ composite-based piezoelectric nanogenerator. Nanomaterials 2018;8:777.

[32] Shi K, Sun B, Huang X, Jiang P. Synergistic effect of graphene nanosheet and $BaTiO_3$ nanoparticles on performance enhancement of electrospun PVDF nanofiber mat for flexible piezoelectric nanogenerators. Nano Energy 2018;52:153–62.

[33] Zhai P, He W, Zeng C, Li L, Yang W. Biomimetic plant-cell composite gel polymer electrolyte for boosting rate performance of lithium metal batteries. Chem Eng J 2023;451:138414.

[34] Wang S, Zhou L, Tufail MK, Yang L, Zhai P, Chen R, et al. In-Situ synthesized Non-flammable gel polymer electrolyte enable highly safe and Dendrite-Free lithium metal batteries. Chem Eng J 2021;415:128846.

[35] Cui Y, Wan J, Ye Y, Liu K, Chou LY. A fireproof, lightweight, polymer–polymer solid-state electrolyte for safe lithium batteries. Nano Lett 2020;20:1686–92.

[36] Shim J, Lee JW, Bae KY, Kim HJ, Yoon WY, Lee JC. Dendrite suppression by synergistic combination of solid polymer electrolyte crosslinked with natural terpenes and lithium-powder anode for lithium-metal batteries. ChemSusChem 2017;10:2274–83.

[37] Wang S, Sun Q, Peng W, Ma Y, Zhou Y, Song D, et al. Ameliorating the interfacial issues of all-solid-state lithium metal batteries by constructing polymer/inorganic composite electrolyte. J Energy Chem 2021;58:85–93.

[38] Wang Z, Zhou H, Meng C, Zhang L, Cai Y, Yuan A. Anion-immobilized and fiber-reinforced hybrid polymer electrolyte for advanced lithium-metal batteries. Chemelectrochem 2020;7:2660–4.

[39] Gao L, Li J, Sarmad B, Cheng B, Kang W, Deng N. A 3D polyacrylonitrile nanofiber and flexible polydimethylsiloxane macromolecule combined all-solid-state composite electrolyte for efficient lithium metal batteries. Nanoscale 2020;12:14279–89.

[40] Wu J, Rao Z, Cheng Z, Yuan L, Li Z, Huang Y. Ultrathin, flexible polymer electrolyte for cost-effective fabrication of all-solid-state lithium metal batteries. Adv Energy Mater 2019;9:902767.

[41] Huang Y, Zhang Z, Gao H, Huang J, Li C. $Li_{1.5}Al_{0.5}Ti_{1.5}(PO_4)_3$ enhanced polyethylene oxide polymer electrolyte for all-solid-state lithium batteries. Solid State Ionics 2020;356:115437.

[42] Zhang X, Wang S, Xue C, Xin C, Lin Y, Shen Y, et al. Self-suppression of lithium dendrite in all-solid-state lithium metal batteries with poly (vinylidene

difluoride)-based solid electrolytes. Adv Mater 2019;31:1806082.

[43] Li Y, Zhang W, Dou Q, Wong KW, Ng KM. $Li_7La_3Zr_2O_{12}$ ceramic nanofiber-incorporated composite polymer electrolytes for lithium metal batteries. J Mater Chem 2019;7:3391–8.

[44] Notes : A1: PI/DBDPE/PEO/LiTFSI, A2: BPT/Allyl PEO/Geraniol, A3: PEO-LLZO-LiTFSI, A4: GF@ZIF@PEO, A5: PEO-LITFSI-PAN/PDMS, A6: PI/PEO/LiTFSI, A7: PEO/LATP, A8: PVDF-LiFSI, A9: PVDF-HFP/LiTFSI/LLZO, Our work: PAN@BTO-S.

[45] Eshetu GG, Judez X, Li C, Bondarchuk O, Rodriguez-Martinez LM, Zhang H, et al. Lithium azide as an electrolyte additive for all-solid-state lithium–sulfur batteries. Angew Chem, Int Ed 2017;56(48):15368–72.

[46] Zheng Y, Li X, Fullerton WR, Qian Q, Shang M, Niu J, et al. Interpenetrating network-based hybrid solid and gel electrolytes for high voltage lithium metal batteries. ACS Appl Energy Mater 2021;4(6):5639–48.

[47] Ma Y, Wan J, Yang Y, Ye Y, Xiao X, Boyle DT, et al. Scalable, Ultrathin, and high-temperature-resistant solid polymer electrolytes for energy-dense lithium metal batteries. Adv Energy Mater 2022;12(15):2103720.

[48] Shi P, Ma J, Huang Y, Fu W, Li S, Wang S, et al. A thin and high-strength composite polymer solid-state electrolyte with a highly efficient and uniform ion-transport network. J Mater Chem 2021;9(25):14344–51.

[49] Shen Z, Zhong J, Jiang S, Xie W, Zhan S, Lin K, et al. Polyacrylonitrile porous membrane-based gel polymer electrolyte by in situ free-radical polymerization for stable Li metal batteries. ACS Appl Mater Interfaces 2022;14(36):41022–36.

[50] Zhao Q, Tu Z, Wei S, Zhang K, Choudhury S, Liu X, et al. Building organic/inorganic hybrid interphases for fast interfacial transport in rechargeable metal batteries. Angew Chem, Int Ed 2018;130:1004–8.

[51] Wang X, Song Y, Jiang X, Liu Q, Dong J, Wang J, et al. Constructing interfacial nanolayer stabilizes 4.3 V high-voltage all-solid-state lithium batteries with PEO-based solid-state electrolyte. Adv Funct Mater 2022;32:2113068.

[52] Liu B, Huang Y, Cao H, Zhao L, Huang Y, Song A, et al. A novel porous gel polymer electrolyte based on poly (acrylonitrile-polyhedral oligomeric silsesquioxane) with high performances for lithium-ion batteries. J Membr Sci 2018;545:140–9.

Dr Haitao Zhang is currently a full professor at the Southwest Jiaotong University. He received his B.S. and M.S. degrees in Materials Science and Engineering from Hainan University from 2008 to 2011; and his Ph.D. degree in Electrical Engineering from the Institute of Electrical Engineering, Chinese Academy of Sciences in 2015. He is a recipient of 100 excellent PhD theses from Chinese Academy of Sciences (2016), and was selected as the Eagle Scholar and Rising Star of Science and Technology in Southwest Jiaotong University in 2017. His research interests focus on the electrochemical energy storage such as Li-ion batteries, supercapacitors, and high-entropy polymer electrolytes. He has published more than 120 SCI papers in top international journals such as Advanced Functional Materials, Nano Today, ACS Nano, Nano Energy, *etc.*.

Hongzhi Peng received his B.S. from Xihua University in 2021. He is currently pursuing M.S. degree in materials science and engineering at Southwest Jiaotong University.